Available online at www.sciencedirect.com
ScienceDirect
Trans. Nonferrous Met. Soc. China 35(2025) 872−887
Transactions of Nonferrous Metals Society of China
www.tnmsc.cn

Superb strength−ductility synergy in Si added metastable high-entropy alloys at cryogenic temperature via reinforced TRIP effect

Zhan-jiang LI[1,2,3#], Yi-xi HOU[4#], Li CHEN[1,2], Qing-xin CHEN[2,3], Jun-feng CHEN[1], Fa CHANG[2,3], Pin-qiang DAI[1,2,3], Qun-hua TANG[5]

1. College of Materials Science and Engineering, Fuzhou University, Fuzhou 350116, China;
2. College of Materials Science and Engineering, Fujian University of Technology, Fuzhou 350118, China;
3. Fujian Provincial Key Laboratory of New Material Preparation and Forming Technology, Fuzhou 350118, China;
4. Beijing Key Laboratory of Microstructure and Property of Advanced Materials, Faculty of Materials and Manufacturing, Beijing University of Technology, Beijing 100124, China;
5. School of Mechanical & Electrical Engineering, Putian University, Putian 351100, China

Received 4 August 2023; accepted 25 April 2024

Abstract: The tensile behavior of $(Fe_{50}Mn_{30}Co_{10}Cr_{10})_{100-x}Si_x$ (x=0 (Si0), 2 (Si2)) metastable HEAs prepared by selective laser melting was studied at cryogenic temperatures. The results demonstrate that the addition of Si leads to lattice distortion and a decrease in stacking fault energy, especially at 77 K, which significantly promotes transformation-induced plasticity (TRIP) in Si2 HEAs. The yield strength, tensile strength, and ductility of Si2 HEAs are 505.2 MPa, 1364.1 MPa, and 19%, which are 43%, 53% and 58% higher than those of Si0 alloy, respectively. TRIP is the main deformation mode, in addition to dislocation slip, and plays a key role in strengthening. The reinforced and continuously sustained TRIP maintains a dynamic strain distribution during deformation. Ultrahigh strain hardening greatly enhances the strength and ductility.

Key words: $Fe_{50}Mn_{30}Co_{10}Cr_{10}$ HEAs; selective laser melting; cryogenic temperature; Si addition; transformation-induced plasticity (TRIP) effect

1 Introduction

Laser selective melting (SLM) is an additive manufacturing technology that overcomes the difficulty of manufacturing metal parts with complex shapes using traditional processes. It can directly form metal parts with nearly full density and good mechanical properties [1]. This expands the scope of high-entropy alloys (HEAs). However, these SLM HEAs have a relatively high yield strength, and their ductility is significantly reduced compared with that of the as-cast comparts [2−4]. To solve this issue, researchers have performed stress-relieving annealing of SLM samples [5]. LIN et al [5] annealed SLM FeCoCrNi HEAs at different temperatures. Although the ductility of the annealed alloy increased, the yield strength decreased significantly compared to that of its cast counterpart. This significantly reduces the advantages of the SLM alloys and limits their engineering applications. Therefore, there is a need to further improve the ductility of SLM high-entropy alloys while maintaining their excellent strength for practical applications.

Generally, the deformation mechanisms of

# Zhan-jiang LI and Yi-xi HOU contributed equally to this work
Corresponding author: Pin-qiang DAI, Tel: +86-18950330431, E-mail: pqdai@126.com; Qun-hua TANG, Tel: +86-13599006251, E-mail: qh_tang@126.com
DOI: https://doi.org/10.1016/S1003-6326(24)66720-8

the twinning-induced plasticity (TWIP) and transformation-induced plasticity (TRIP) are obtained by tailoring the stacking fault energy (SFE) and phase stability, which provides a method for metallic materials to overcome the strength-ductility trade-off [6]. Therefore, the design of HEAs based on low SFE and phase stability strategies has been widely studied [7], as has been shown for different HEAs based on the Fe−Mn−Co−Cr system [8,9]. Unexpectedly, a synergy between the strength and ductility was achieved. CoCrNi and iron-based $Fe_x(CoNi)_{90-x}Cr_{10}$ (at.%) alloy systems are among the best candidates because of their low SFE and high sensitivity to phase transitions caused by compositional changes [10,11]. This concept also applies to SLM-HEAs because of their high ductility. Solute inhomogeneity (cell structure) in SLM alloys can influence the deformation mechanism by changing the local composition and phase stability [12], which is also frequently reported in conventional additive manufacturing steels [13]. However, most of these studies focused on the mechanical properties at room temperature.

To further develop and expand the potential of SLM-HEAs in the industrial applications, the performance of SLM-HEAs at the cryogenic temperatures should be considered. Excellent properties of the as-cast HEAs at cryogenic temperatures have been demonstrated [14], mainly because the cryogenic temperature reduces the SFE of the alloy [15]. The deformation mode of an alloy at cryogenic temperatures changes from plane-slip dislocation activity at room temperature to deformation twinning and phase transformation, resulting in continuous and stable strain hardening [14]. Owing to the large residual stress produced by rapid solidification during the SLM process, the printed samples were more brittle than the cast samples [16]. Therefore, it is important to understand the performance of SLM-HEAs at cryogenic temperatures.

In this work, a non-equiatomic $Fe_{50}Mn_{30}Co_{10}Cr_{10}$ HEA was chosen as the alloy for the study. Previous studies have found that as-cast $Fe_{50}Mn_{30}Co_{10}Cr_{10}$ HEAs possess an excellent combination of strength and ductility owing to their phase transformation-induced plasticity (TRIP) and twinning-induced plasticity (TWIP) [11], which are more likely to occur in low-SFE alloys. Based on this, we previously prepared $Fe_{50}Mn_{30}Co_{10}Cr_{10}$ HEAs by SLM [17], and the results were expected to be lower than those of the as-cast alloys reported in the literature. Therefore, a strategy to enhance the strain-hardening ability and improve ductility by reducing the SFE was implemented by adding Si. The addition of Si reduces the SFE of the alloys, which has been demonstrated in CoCrNi alloys [18]. Our previous study also demonstrated that Si can reduce the SFE of $Fe_{50}Mn_{30}Co_{10}Cr_{10}$ HEAs. These results were also confirmed by some studies [18,19], where Si-added alloys achieved a simultaneous increase in strength and ductility compared with Si-free alloys. Therefore, it can be concluded that it is feasible to improve the ductility of SLM-HEAs by reducing the SFE. The SFE of the alloy can be reduced in the cryogenic temperature environment mentioned above; however, the alloy can also become brittle at cryogenic temperatures. Therefore, clarifying the mechanical behavior of SLM-HEAs at cryogenic temperatures is of great significance for practical applications. The purpose of this study is to elucidate the mechanical behavior of Si-added $Fe_{50}Mn_{30}Co_{10}Cr_{10}$ HEAs at cryogenic temperatures.

2 Experimental

2.1 Alloy preparation

Commercially available $Fe_{50}Mn_{30}Co_{10}Cr_{10}$ HEAs spherical powders prepared by gas atomization and irregularly shaped Si powders were used as the starting materials. The powder composition and morphology have been described in previous studies [17]. Si-free samples of ($Fe_{50}Mn_{30}Co_{10}Cr_{10}$) (Si0 HEAs) were prepared directly via HEAs powder printing. The HEAs powders of the Si-added (($Fe_{50}Mn_{30}Co_{10}Cr_{10}$)$_{98}Si_2$) (Si2 HEAs) samples were first mixed with Si powders for 24 h in a roller ball mill before printing. The morphology and elemental distribution of the mixed powders of the Si0 and Si2 samples are shown in Fig. 1. Microstructural characterization samples (10 mm × 10 mm × 2 mm) and tensile test samples (10 mm × 2 mm × 1 mm) were printed on the same substrate using a German SLM-Solution 125 HL metal 3D printer under an argon atmosphere. The optimal printing parameters were 220 W of laser power, 40 μm of layer thickness, 60 μm of hatching space, and 1000 mm/s of scanning speed, respectively.

2.2 Microstructural characterization and tensile test

The microstructures were characterized using X-ray diffraction (XRD, D8 Advance, Germany), scanning electron microscopy (SEM, FEI Nova Nano SEM 450, USA), electron backscatter diffraction (EBSD, HKL Channel 5 Oxford, UK), and transmission electron microscopy (TEM, FEI Talos F200X, USA). Among them, in order to avoid the influence of surface stress-induced phase transition caused by mechanical polishing on the test results, the XRD pattern was tested after electrolytic polishing. XRD was performed using a Cu K_α ray operated at a tube current of 40 mA and tube voltage of 40 kV. EBSD samples were prepared by electropolishing in an ethanol (77%)–perchloric acid (23%) solution. The TEM samples were prepared by mechanical grinding and ion-beam thinning (Gatan 691, USA). The cryogenic temperature tensile test was performed using a universal testing machine (INSTRON2382, USA) at a strain rate of 1×10^{-3} s^{-1}.

3 Results

3.1 Powder characterization

Before preparing the alloy block, the alloy powder was characterized using SEM. Figure 1(a) shows the $Fe_{50}Mn_{30}Co_{10}Cr_{10}$ HEAs powder prepared via gas atomization. The powders are composed of a high proportion of near-spherical particles and relatively few irregularly shaped particles. In addition, many small satellite particles were attached to the surfaces of a small number of particles. The formation of satellite particles was caused by collisions between solidified droplets during gas atomization.

The presence of these irregularly shaped and satellite particles did not adversely affect the printing of the HEA powder. Figure 1(b) shows a high-resolution SEM image of a single spherical powder. The corresponding elemental distribution

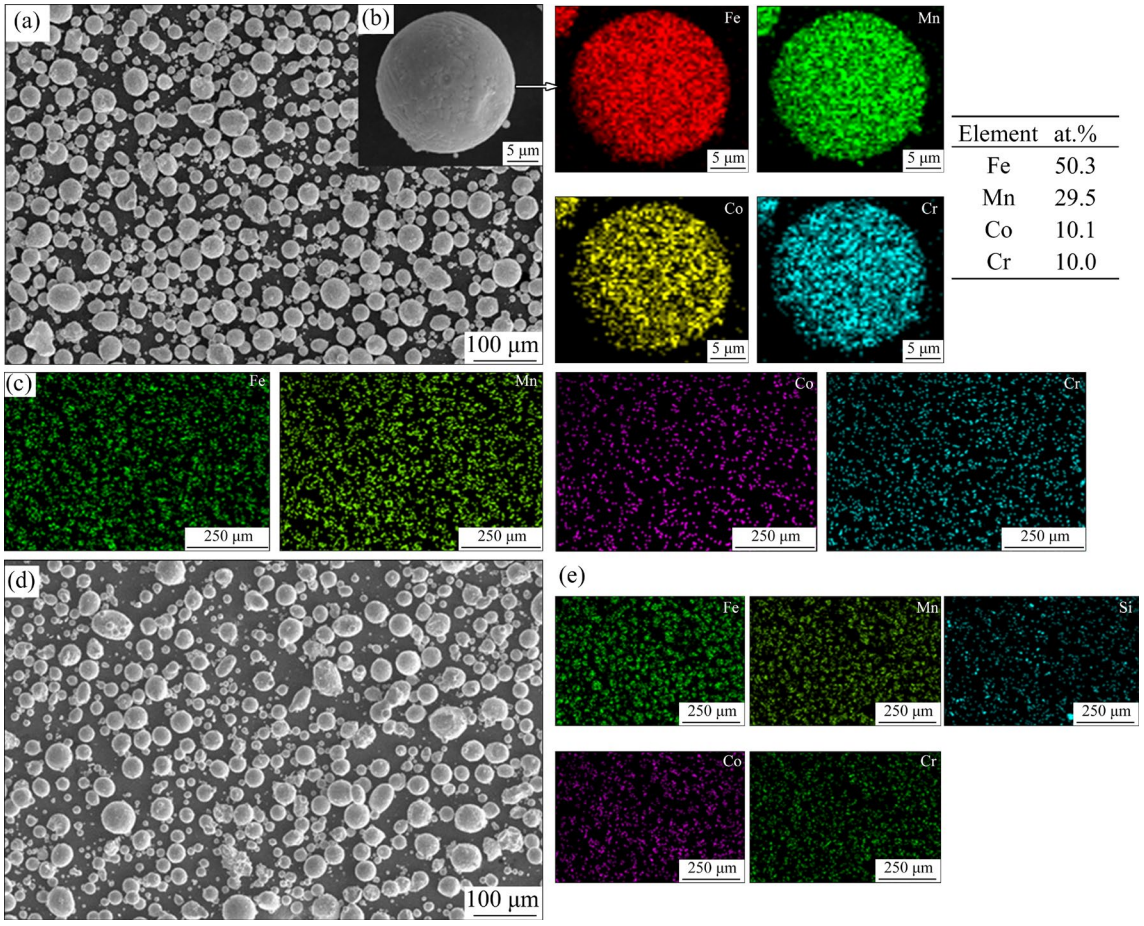

Fig. 1 Analysis of SLM-HEAs powders: (a) Low magnification SEM micrograph of Si0 HEAs; (b) High magnification SEM micrograph and elemental distribution maps of single powder particle; (c) EDS elemental distribution maps of Si0 HEAs; (d) Low magnification SEM micrograph of Si2 HEAs; (e) EDS elemental distribution maps of Si2 HEAs

maps obtained by EDS analysis (Figs. 1(b) and (c)) show that the elemental distribution is relatively homogeneous without obvious segregation, and the chemical composition is consistent with the design composition. The HEA mixed powder after the addition of Si is shown in Fig. 1(d). It can be seen that the particle size and shape of the powder remained almost unchanged after 24 h of mechanical mixing, which also facilitated the successful preparation of the subsequent alloy blocks. EDS analysis (Fig. 1(e)) of the Si2 HEAs mixed powder showed that the Si particles were successfully dispersed between the matrix powders without obvious agglomeration. In addition, the XRD phase analysis in Fig. 2 shows that the Si0 and Si2 HEA powders are mainly composed of the FCC phase, and the peak of Si is not detected, mainly because of its small content.

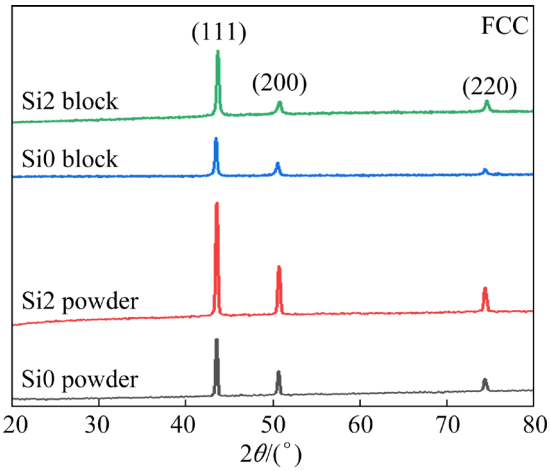

Fig. 2 XRD patterns of SLM-HEA powders and block

3.2 SLM-HEAs block

SEM images of the SLM-HEA block are shown in Fig. 3. The 3D metallographic and low-resolution SEM images (Figs. 3(b) and (d)) show that SLM-HEA has a typical fish-scale layered structure. The high-resolution SEM microstructure is shown in Figs. 3 (a) and (c), and small elongated columnar substructures (width ~1 μm) are observed inside the grains. The TEM image (inset in Fig. 3(d)) shows many dislocation cell substructures with dense dislocations arranged in the walls surrounding the cells. This was also observed in several SLM-prepared HEAs [20−22]. These dislocation cells

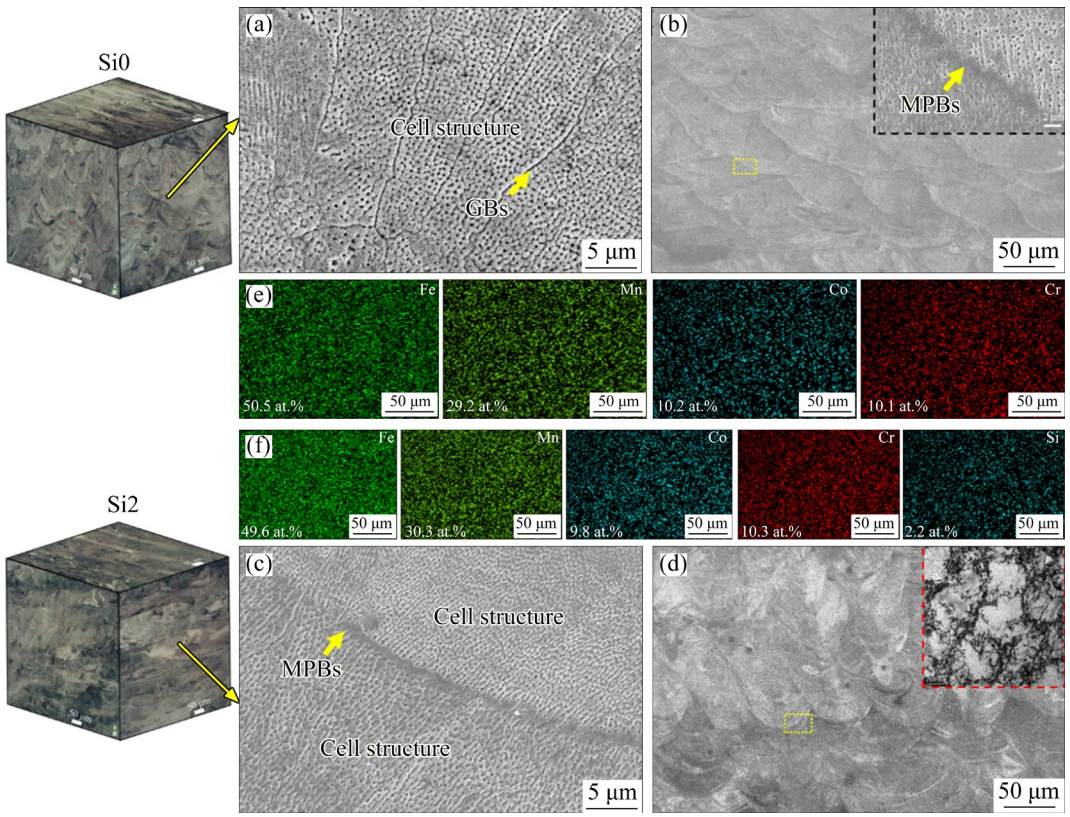

Fig. 3 SEM images of SLM-HEA block: (a, b) Si0 HEAs; (c, d) Si2 HEAs; (a, c) Top surface; (b, d) Side surface; (e) EDS elemental distribution maps of Si0 HEAs; (f) EDS elemental distribution maps of Si2 HEAs (Insets (top right corner) of (b) and (d) are high magnification micrographs)

are called dislocation networks and are also the walls of substructures. The formation of these high-density dislocation walls was mainly attributed to the retention of more vacancies during the rapid solidification process [20]. The EDS mapping analysis showed that the elemental distribution of the SLM-HEA was uniform without obvious segregation, and the chemical composition of the elements was consistent with the design. In addition, XRD tests showed that the phase composition of the SLM-HEA was still single-phase FCC (Fig. 2).

3.3 Tensile test at cryogenic temperatures

The engineering stress−strain curves of the Si0 and Si2 HEAs at cryogenic temperatures (77 K) are shown in Fig. 4(a). It can be seen that the yield strength, tensile strength and fracture elongation of Si2 HEA are vastly higher than those of Si0 HEA. The yield strength, tensile strength, and fracture elongation of Si2 HEAs are 505.2 MPa, 1364.1 MPa, and 19%, respectively. The tensile strength and ductility of Si2 HEAs were improved by 53.1% and 58% respectively compared with those of Si0 HEAs. The significant improvement in strength and ductility may be mainly attributed to the decrease in SFE owing to Si addition and the cryogenic temperature environment [15,18]. Generally, for high-SFE alloys, although conventional strengthening mechanisms such as precipitation strengthening and dislocation strengthening can significantly improve the yield strength, the ductility and tensile strength are lower, particularly in cryogenic temperature environments. This is mainly attributed to two reasons: the probability of deformation mechanisms such as laminar dislocations and twinning, and martensitic transformation is lower in high-SFE alloys than in low-SFE alloys [23], and dislocation motion is suppressed in low-temperature environments [24].

The excellent combination of strength and ductility of the SLM-Si2 HEAs in this study was inseparable from their special strain-hardening mechanism. Compared to the Si0-HEAs, micro-sized dimples were observed on the fracture surface of the Si2 HEAs (see Figs. 4(c) and (d)), which confirmed the excellent ductility of the alloy at cryogenic temperatures. Figure 4(b) shows the strain-hardening responses of the Si0 and Si2 HEAs during the cryogenic temperature tensile tests. The strain-hardening rates of the Si2 HEAs were much higher than those of the Si0 HEAs. A higher strain-hardening capability is a key factor for Si2 HEAs to achieve a synergistic increase in strength and ductility in all strain processes. This strain-

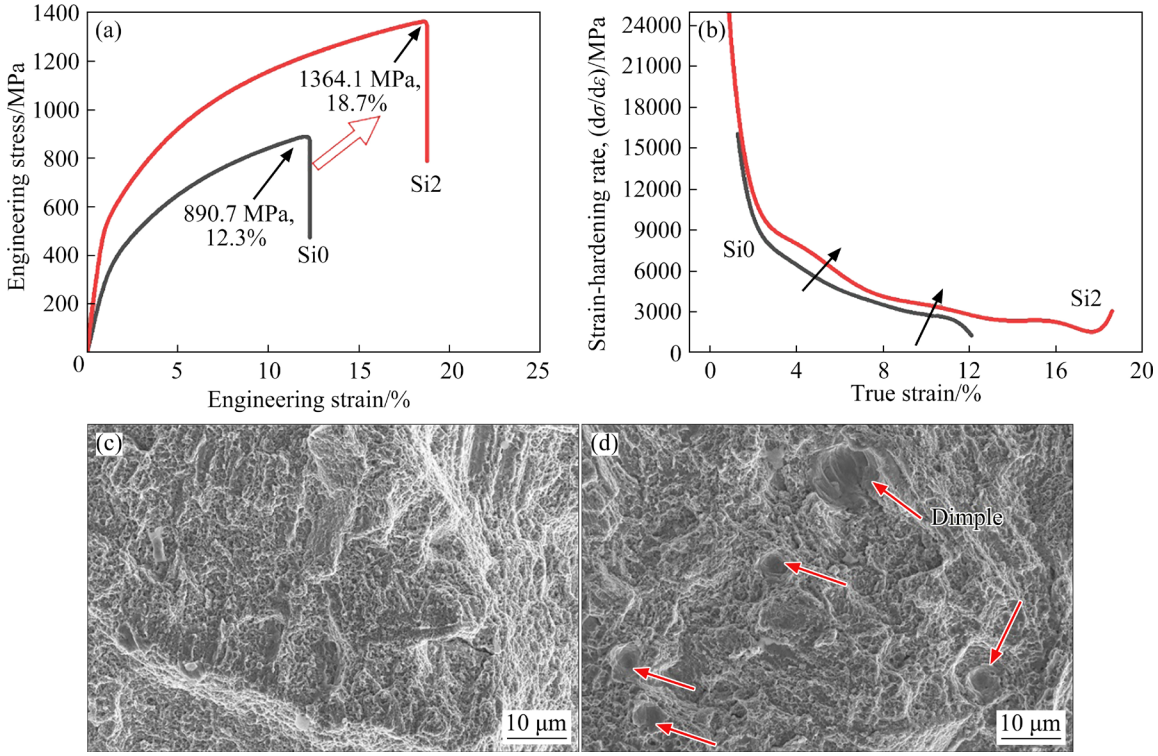

Fig. 4 Cryogenic temperature tensile properties of SLM-HEAs at 77 K: (a) Engineering stress−engineering strain curve; (b) Strain-hardening rate curve; (c, d) Fracture surfaces morphology of Si0 and Si2 HEAs, respectively

hardening behavior is attributed to the extremely high extent of deformation-driven phase transformation. The tensile properties also proved that the SLM-HEA did not become brittle at cryogenic temperatures, even though its ductility at room temperature was lower than that of the as-cast state [17].

3.4 Microstructure evolution in deformation process

To clarify the plastic deformation mechanism of the Si0 HEAs and Si2 HEAs at 77 K, the evolution of the deformation substructures under different interruption strains was analyzed using EBSD and TEM. The high strain-hardening ability of Si2 HEAs overcomes the strength-ductility trade-off. Therefore, it is crucial to clarify the corresponding tensile deformation mechanism. An EBSD analysis was performed on the different interruption strains, as shown in Fig. 5. Figures 5(b−d) show the interruption at strains of 5%, 10% and fracture for Si0 HEAs. Figures 5(f−i) show the interrupted at strains of 5%, 10%, 15%, and fracture for Si2 HEAs. The EBSD results for the two HEA without strain are shown in Figs. 5(a) and (e). The IPF and phase distribution maps of the two alloys during deformation show that the volume fraction of the HCP phase gradually increases with an increase in strain. This preliminary shows that the deformation induced martensitic transformation (FCC→HCP) is the main deformation mechanism of the SLM-HEA. For Si0 HEAs, the volume fraction of HCP phase increased from 0% to 11.3% as the strain increased from 0% to fracture (13%). For Si2 HEAs, when the strain was 10%, the volume fraction of HCP phase reached 18%, which was significantly higher than that of Si0 HEAs. As the strain further increased, the volume fraction of HCP phase of Si2 HEAs increased continuously until it reached 32.8% at fracture. During deformation, the volume fraction of the HCP phase transformation produced in Si2 HEAs was significantly higher than that produced in Si0 HEAs. It was found that the secondary phase and twins generated during the deformation process significantly increased the interface density of the alloy, which increased the additional dislocation slip barriers, thereby increasing strain hardening [11,25].

For the Si0 and Si2 samples deformed at 77 K, the evolution of the dislocation density at the sequential strain level was preliminarily characterized by the EBSD method. Figures 6 and 7 show the geometrically necessary dislocation (GND) maps of Si0 alloy were 10% strain and 12% strain (fracture), whereas GND maps of Si2 alloy were 10% strain, 15% strain, and 19% strain (fracture). GND is typically produced to accommodate the strain gradients during heterogeneous deformation [27].

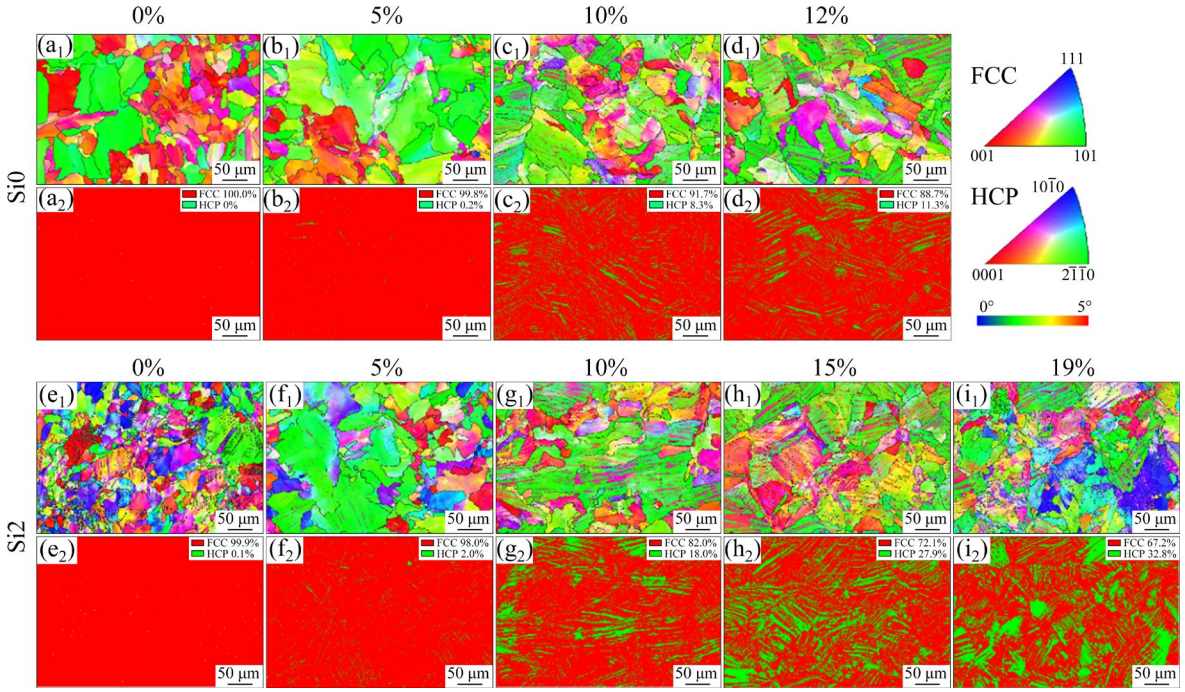

Fig. 5 IPF diagrams (a_1−i_1) and phase distribution diagrams (a_2−i_2) of SLM-HEAs

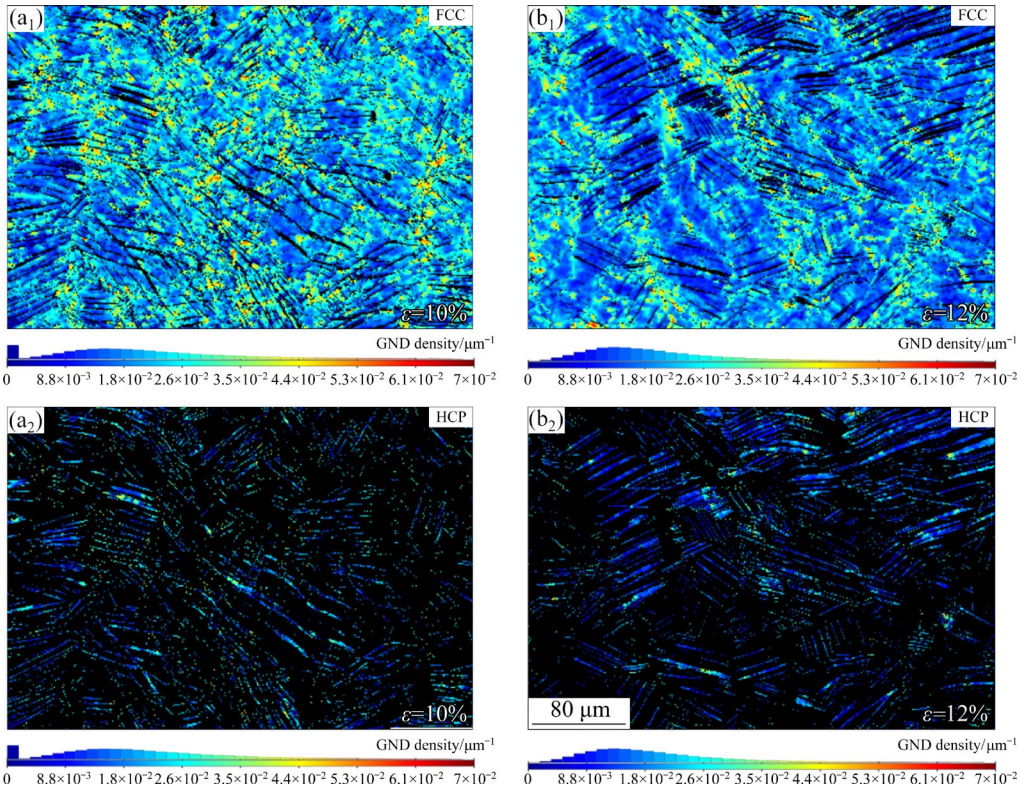

Fig. 6 EBSD GND maps of FCC phase (a_1, b_1) and HCP martensite (a_2, b_2) at different local strains of SLM-processed Si0 HEAs (The color bar in GND maps indicates the range of GND density; These raw data were done with the ATEX software [26])

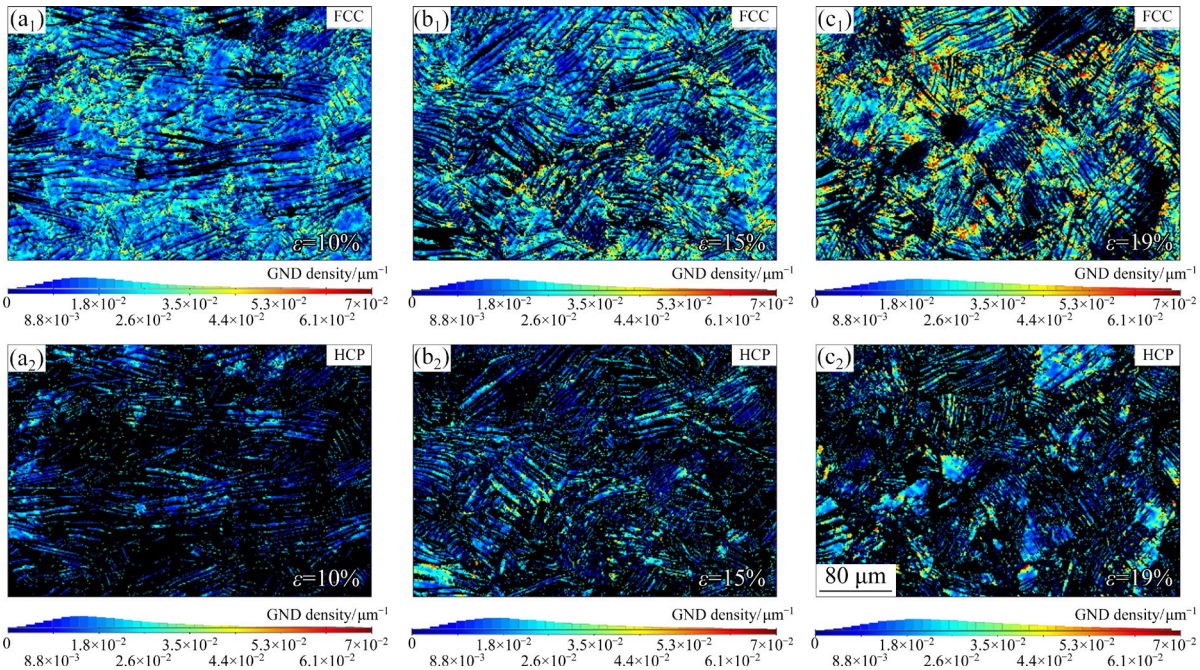

Fig. 7 EBSD GND maps of FCC phase (a_1, b_1, c_1) and HCP martensite (a_2, b_2, c_2) at different local strains of SLM-processed Si2 HEAs (The color bar in GND maps indicates the range of GND density)

For Si0 HEAs, the difference in GND was not obvious because of similar strains (10% and 12%). For the Si2 HEAs, it can be clearly observed that the GND increases significantly with increasing strain. Notably, as the strain increases, the GND of both the FCC and HCP phases increases, indicating that both phases can regulate plastic deformation. After the HCP martensite phase appeared, the soft

FCC phase could accommodate a larger plastic strain than the HCP phase, thereby producing strain partitioning [28]. With an increase in strain, the volume fraction of the HCP phase increased, and there were more phase interfaces, which increased the hindrance to dislocations and thus led to a higher GND. It was also found that the GND around the FCC and HCP phase interfaces were higher than those inside the phase interface. This was mainly due to the increase in the volume fraction of the hard HCP phase, which resulted in a serious mismatch in the strength level of the system and serious incompatibility in plasticity. As the strain increased, the GND at the FCC phase boundary rapidly evolved to adapt to the high strain gradient and maintain physical compatibility. As the strain continued, the volume fraction of martensite increased, which led to a severe evolution of the GND at the phase interface.

In other words, dynamic stress−strain partitioning occurred to alleviate the mechanical incompatibility between the FCC and HCP phases. This was accompanied by the active evolution of the GND density at the phase boundary, which led to rapid strain hardening through high back stress evolution [28]. Consequently, with an increase in the strain, the volume fraction of the HCP phase in the maximum deformation region was the highest based on the effect of TRIP, which gradually hardened the region. The region adjacent to the maximum deformation region can be regarded as a softer region, and the strain localization can move to this region. Similarly, an HCP phase transition can also be triggered in the new deformation region. During plastic deformation, this phenomenon can be transferred from the center of the large deformation area to the edge. Thus, the total volume fraction of martensite in the tensile specimen increased sharply during plastic deformation, which promoted the sequential strain-hardening behavior of the SLM-processed HEA during tensile deformation [12,26].

To further characterize the microstructural evolution during the deformation process and clarify the deformation mechanism, the TEM images of the Si0 HEAs after fracture and the Si2 HEAs after 10% intercept and fracture are shown in Fig. 8. Regarding the TEM microstructure of Si0 HEAs after fracture, a large number of slatted HCP phases with an average spacing in the range of 34.3 μm and dislocation cells (DCs) were found, which is consistent with the EBSD test results. High-density dislocation walls (HDDWs) derived from dislocations generated by dislocation slip were also observed (Figs. 8(a_2) and (a_3). A large number of accumulated high-density dislocation (HDDs) zones were found around the HDDWs, which is apparently a HDDWs impeding the dislocation slip. A small number of microbands (MBs) were also observed (Fig. 8(a_2)), which were caused by the planar slip of dislocations. The microbands formed during the early deformation also impede the slip of subsequent dislocations. Owing to the extensive interaction between the layer dislocations and HCP slats, Lomer-Cottrell (L-C) lock defect derivatives were formed, which are similar to the L-C lock formed in the microstructure of $(NiCoCr)_{92}Al_6Ta_2$ medium-entropy alloys deformed 63% at 77 K [29]. Interestingly, compared with room temperature, the deformation twins (DTs) of the alloys were greatly reduced at cryogenic temperatures, with only very small amounts, as shown in Fig. 8(a_3). The reduction in DTs during cryogenic temperature deformation is mainly attributed to a decrease in the SFE, which has been reported for both stainless steels and HEA [30].

In contrast, the deformed substructures of Si2 HEAs at 10% strain and after fracture were observed using TEM. At the 10% strain level, in agreement with the EBSD test results, slatted HCP was found, and the average width was about 106.2 μm, which is much larger than the width of the HCP phase in Si0 HEAs after fracture. A large accumulation of HDDs is also observed around the HCP phase, indicating that the HCP phase boundary effectively hinders the slipping of dislocations. Another parallel arrangement of stacking faults (SFs) was observed, which is usually the basis of the HCP phase transformation. Interestingly, a large number of planar slip bands were observed, which was unexpected relative to the very small number of MBs in the Si0 HEAs fracture. This indicates that the addition of Si had a significant effect on the deformation behavior of the alloy. The discovery of a large number of MBs indicates that the Si2 HEAs were dominated by planar slip during the early stages of deformation. In addition, subgrain dislocation boxes (SDBs) consisting of mutually perpendicular MBs were also observed, suggesting a significant interaction between slip systems. Specifically, this so-called “microbands-

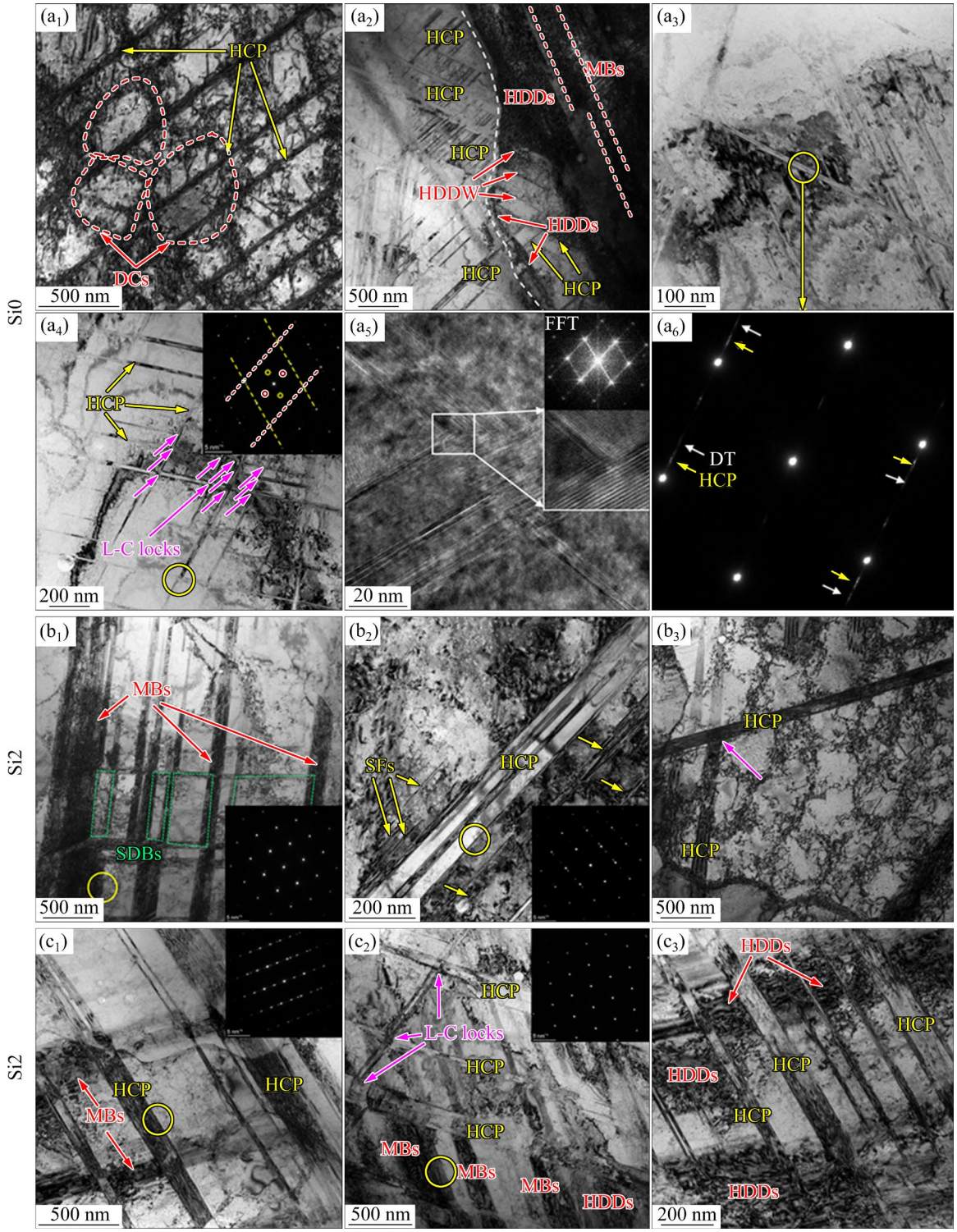

Fig. 8 Typically deformed substructures of SLM-HEAs at 77 K showing microstructural evolution with different local strains: (a) 12%; (b) 10%; (c) 19%

parallel hexahedral" stability defect is formed by the interaction of two partial dislocation systems sliding in different {111} planes [31]. Numerous slatted HCP phases and planar-slip MBs were produced when the strain increased to fracture, and the average thickness of the HCP phases was approximately 118.0 μm. In addition, many blocked microbands were found between the parallel HCP phases, indicating that the HCP phase boundary obstructed the planar slip of the dislocations. Similarly, L-C locks formed by the intersection of slatted HCP phases were also found. The deformed

microstructures found in Si2 HEAs and the differences with Si0 HEAs further suggest that the addition of Si affects dislocation slip and the formation of HCP phases in the alloy. There is no doubt that the addition of Si reduces the SFE of the alloy, which is the main reason for the differences in the deformation microstructures [18,19,32].

4 Discussion

4.1 SFE-dependent deformation mechanisms

The above EBSD and TEM characterization results show that the plastic deformations of the Si0 and Si2 HEAs are significantly different, with the latter having more dislocation plane slip bands (MBs) and a thicker deformed HCP lath. Clearly, the addition of Si makes the SLM-HEA more prone to planar slip and the TRIP effect, and it is clear that the difference is mainly attributed to the reduction in SFE in HEAs by Si addition. For Si2 HEAs, more microbands and HCP phases cause considerable additional interfaces, which play a key role in improving the strength, ductility, and strain-hardening ability [11]. This provides an important basis for Si2 HEAs to achieve excellent mechanical properties. The SFE refers to the energy consumed by the shearing of one atomic plane relative to another; therefore, it is directly related to the response of a crystal to deformation [33]. Particularly in FCC crystals, the level of SFE affects the mobility of dislocations, the ability to cross slip, and the formation of twins, all of which determine the mechanical behavior. With a decrease in the SFE, the deformation mechanism gradually shifts from a single dislocation slip to multiple mechanisms (dislocation slip, twinning (TWIP effect), followed by HCP martensitic phase transition (TRIP effect)). Therefore, the decrease in SFE inhibited the cross-slip of dislocations and promoted the occurrence of the HCP phase transition. The negative SFE of the FCC phase configuration indicates that HCP stacking is beneficial for the stability of the structure [34]. In other words, the HCP phase is more favorable in terms of energy, whereas the FCC phase is metastable at a lower SFE, which is favorable for the FCC-to-HCP transition.

In addition, in previous research (room temperature) [17], the main deformation mechanisms of Si-added alloys were twinning and martensitic phase transformations. In this study, at cryogenic temperatures, the deformation mechanism was dominated by the martensitic phase transformation, which was mainly attributed to the much lower SFE [30,35]. This is similar to the results of a study on austenitic stainless steels by LI et al [35]. Because of the very low SFE, the samples deformed at 15 and 50 K were more susceptible to phase transformations, whereas the samples deformed at 173 K formed both deformation twins and phase transformations. Thus, the deformation mechanism changed as the SFE decreased. These results clearly show that different transformation mechanisms operate at different temperatures, and that the operating deformation mechanism strongly depends on the SFE. Since lower SFE materials show wider stacking faults and are more difficult to cross-slip [36], with decreasing SFE, stacking faults tend to overlap on every second (111) planes, reducing the overall energy of these stacking fault bundles to form ε-martensite. This can explain why more ε-martensite is formed from γ-austenite with decreasing temperature.

To prove this, the concept of an effective energy barrier (EEBs) [37] is used to quantify the competition between twinning (TW) and FCC-HCP martensitic transformation (MT), as follows:

$$\overline{\gamma}_{\mathrm{MT}}(\theta)=\frac{\gamma_{\mathrm{usf}}^{\mathrm{fcc}}}{\cos\theta} \tag{1}$$

$$\overline{\gamma}_{\mathrm{TW}}(\theta)=\frac{\gamma_{\mathrm{utf}}^{\mathrm{fcc}}-\gamma_{\mathrm{isf}}^{\mathrm{fcc}}}{\cos\theta} \tag{2}$$

where $\overline{\gamma}_{\mathrm{MT}}$ and $\overline{\gamma}_{\mathrm{TW}}$ are the EEBs for MT and TW, respectively; $\gamma_{\mathrm{usf}}^{\mathrm{fcc}}$, $\gamma_{\mathrm{isf}}^{\mathrm{fcc}}$ and $\gamma_{\mathrm{utf}}^{\mathrm{fcc}}$ are unstable SFE, intrinsic SFE, and unstable twinning fault energy, respectively; θ ($0°\le\theta\le60°$) is the effect of crystal orientation on the activation of the deformation mode, and θ ($0°\le\theta\le60°$) is measured by the angle between the decomposition shear stress and the twin direction [38]. Regarding the negative intrinsic SFE ($\gamma_{\mathrm{isf}}^{\mathrm{fcc}}=-31$ mJ/m^2) of the $Fe_{50}Mn_{30}Co_{10}Cr_{10}$ HEAs, SF formation is superior to twinning in a large θ range. Here, the twin energy barrier was defined based on the classical twin route [37]. According to the Schmidt's law, dislocation slip can always be activated at large θ values. Then, the boundary between FCC→HCP MT and TW is given by $\overline{\gamma}_{\mathrm{TW}}(\theta)=\overline{\gamma}_{\mathrm{MT}}(\theta)$. In FCC alloys, unstable twinning fault energy, unstable SFE and intrinsic SFE usually have the following relationship, i.e.,

$\gamma_{utf}^{fcc} \approx \gamma_{usf}^{fcc}+1/2\gamma_{isf}^{fcc}$. Therefore, when the intrinsic SFE is more negative, the EEBs of TW are greater than those of MT. In this case, the alloy is more prone to MT during deformation, whereas TW is inhibited. The addition of Si reduces the SFE of $Fe_{50}Mn_{30}Co_{10}Cr_{10}$ HEAs, which makes the SFE of Si2-HEAs more negative (<−31 mJ/m^2), that is, more deformed HCP martensite will appear. In addition, a two-step twinning process was used to understand the relationship between (negative) SFE and TW [39]. The key parameters controlling the above two steps are $\delta=(\gamma_{usf}^{hcp}-\gamma_{usf}^{fcc})/\gamma_{usf}^{fcc}$ [40]. Based on the relationship between HCP and FCC, as a first-order approximation, there are also $\gamma_{usf}^{hcp} \approx \gamma_{usf}^{fcc}-\gamma_{isf}^{fcc}$. $\delta \approx -\gamma_{isf}^{fcc}/\gamma_{usf}^{fcc}$ also be obtained [39]. Where γ_{usf}^{hcp} is the unstable SFE in the HCP basal plane. With the increase of δ, it becomes more and more difficult to activate partial dislocations in HCP martensite, that is, a larger critical decomposition shear stress is required than the partial dislocations in FCC matrix. Meanwhile, the HCP phase is retained in the deformed structure, and the alloy is deformed by FCC → HCP MT. Of course, this situation is more likely to occur with the decrease of SFE.

To further reveal that Si2-HEAs possess easier FCC-HCP MT capabilities than Si0-HEAs, thermodynamic driving forces were used. In this study, Fig. 4 shows that the addition of Si significantly increased the MT rate of HEA because the addition of Si significantly reduced the FCC phase stability and promoted the formation of HCP martensite. Similar to the study of $Fe_x(CoNi)_{90-x}Cr_{10}$ system HEAs by BAE et al [41], i.e., the elevated Fe content reduces the phase transformation driving force ($\Delta G^{\gamma-\varepsilon}$) of FCC-BCC and promotes the formation of BCC martensite phase during deformation. In thermodynamics, the $\Delta G^{\gamma-\varepsilon}$ of FCC-HCP can be given by Eq (3):

$$\Delta G^{\gamma-\varepsilon}=\sum_i X_i \Delta G_i^{\gamma-\varepsilon}+\frac{1}{2}\sum_{ij} X_i X_j \Delta \Omega_{ij}^{\gamma-\varepsilon} \quad (3)$$

where X_i and $\Delta G_i^{\gamma-\varepsilon}$ are the molar fraction and the difference of free energy between FCC and HCP of pure metals, respectively, and $\Delta \Omega_{ii}^{\gamma-\varepsilon}$ is an interaction energy parameter for components i and j. The corresponding thermodynamic parameters at 298 K are presented in a previous study [17]. Based on Eq. (3), the values of $\Delta G^{\gamma-\varepsilon}$ at 298 K could be thermodynamically estimated to be −237.1 and −279.1 J/mol, respectively, for the of Si0 and Si2 HEAs. The addition of Si increased the phase transformation driving force of FCC-HCP.

4.2 Strengthening mechanisms

As mentioned in Section 3.3, the yield strength of the Si2 HEAs was 150 MPa higher than that of the Si0 HEAs at 77 K. This may be mainly attributed to the lattice distortion caused by the addition of Si, which leads to an improvement in solid solution strengthening. The large lattice distortion caused by the addition of large Si atoms produced a higher barrier at cryogenic temperatures, which increased the yield strength [29]. To further analyze the reason for the high yield strength of the Si2 HEAs, the strengthening model (4) can be applied [42].

$$\sigma_{ys}=\sigma_0+\sigma_{ss}+\sigma_{gb}+\sigma_{dis} \quad (4)$$

where σ_0 is lattice friction stress, and σ_{ss} is solid solution strengthening. In the current analysis, the contribution of σ_{ss} can be incorporated into the friction stress σ_0 [43]. $\sigma_{gb}=Kd^{-1/2}$ is grain boundary strengthening, where K and d are the grain-boundary strengthening coefficient and average grain size, respectively. Here, the K is determined to be 573 MPa/μm$^{1/2}$ according to Ref. [44], which is commonly used for Si0 and Si2 MEAs. The average grain sizes of the two alloys were obtained from the EBSD data analysis shown in Fig. 4, that is, 13.4 μm of Si0 and 8.9 μm of Si2 HEAs. The contribution of grain boundary strengthening of Si0 and Si2 HEAs are 156.5 and 192.0 MPa, respectively. $\sigma_{dis}=\alpha MGb\sqrt{\rho}$ is dislocation strengthening, where α is a constant (0.2) [45], M is the Taylor factor (3.06) accounting for the crystallographic texture, G is the shear modulus (~80 GPa) [43], and b is the component of Burgers vector ($\sqrt{2}/2\times a$ (lattice parameters)) [46]. The values of the Si0 and Si2 HEAs obtained by XRD (Fig. 2) fitting were 0.355 and 0.359 nm, respectively; thus, the b values of the two alloys were 0.251 and 0.254 nm, respectively. And, ρ, average dislocation density, is calculated by XRD measurements according to the Williamson–Hall equation: $\rho=16.1\varepsilon^2/b^2$. Here, ε is the microstrain obtained by $(\delta\cdot\cos\theta/\lambda)/(4\sin\theta)/\lambda$ [45,47−49], where δ represents the true XRD peak broadening. $\delta=\sqrt{\delta_m^2-\delta_0^2}$, where δ_m and δ_0 are the peak

broadening of the test sample and single Si sample, respectively, θ is the Bragg angle of a certain peak, and λ is the wavelength of the X-rays. The ρ and dislocation strengthening of Si0 and Si2 HEAs are respectively 1.06×10^{14} m^{-2}, 128.03 MPa and 1.27×10^{14} m^{-2}, 139.59 MPa. Therefore, σ_0 (Si0: 77.1 MPa, Si2: 173.6 MPa) can also be obtained by subtracting σ_{gb} and σ_{dis} from σ_{ys}.

It can be seen that the higher yield strength of Si2 alloy than that of Si0 alloy is mainly due to the contribution of lattice friction stress. This further confirms that the increase in yield strength is mainly due to the enhancement of the lattice friction stress when Si is added, compared with Si-free HEAs. In fact, at cryogenic temperatures, the available thermal fluctuations are not enough to help dislocations overcome obstacles, so the increase of flow stress drives dislocation motion, resulting in the enhancement of σ_0. The addition of Si enhances the lattice distortion, which requires a higher critical stress to drive the dislocation slip [29]. That is to say, for Si2 HEAs, the higher lattice distortion leads to higher thermal components in yield stress at cryogenic temperatures, promoting a notable increment of σ_{ys}.

4.3 Mechanisms of superior strain hardenability

In this work, SLM $Fe_{50}Mn_{30}Co_{10}Cr_{10}$ metastable HEAs are not only non-brittle at 77 K, but also have significantly improved tensile strength and ductility by adding Si. This is closely related to the deformation mechanism. Figure 9 shows schematic sketches of the deformation mechanism transitions for Si0 and Si2 HEAs at 77 K. It can be seen that the potential microstructural origin is mainly attributed to the simultaneous operation of multiple defects during tensile deformation, including dislocations, SFs, MBs, ε-HCP, and L-C locks, as well as extensive interactions between them. For Si2-HEAs, the rapid generation of these multiple defects and a higher volume fraction play major roles in their excellent strain-hardening ability. The GND diagram of Fig. 7 and the TEM results of Fig. 8 show that the higher strain hardening rate of Si2-HEAs is attributed to the increase of dislocation density and the interaction between dislocation and ε-HCP. This suggests that the increase in the strength of Si2-HEAs is not only due to an increase in the dislocation density, but more importantly to an increase in the volume fraction of ε-HCP. More specifically, the GND density at the interface between austenite and martensite was significantly higher than that inside the austenite and martensite (Figs. 6 and 7). Moreover, this feature was more significant in the Si2 alloy than in the Si0-HEAs.

The EBSD results of the deformed samples in both alloys also confirm that MT is the main additional plastic mode in addition to dislocation slip, which is the key microstructural origin that significantly improves the strength/ductility and excellent strain hardening ability. In general, MT, in addition to serving as a barrier hindering dislocation motion, can also induce grain refinement by introducing additional interfaces, similar to deformation twins, thereby significantly reducing the average free path of dislocations and resulting in an obvious dynamic H−P effect [50]. Another noteworthy result is that, in both alloys, the yield stress increased with addition of Si, which caused the FCC−HCP MT to occur earlier in the deformation (high phase transformation driving

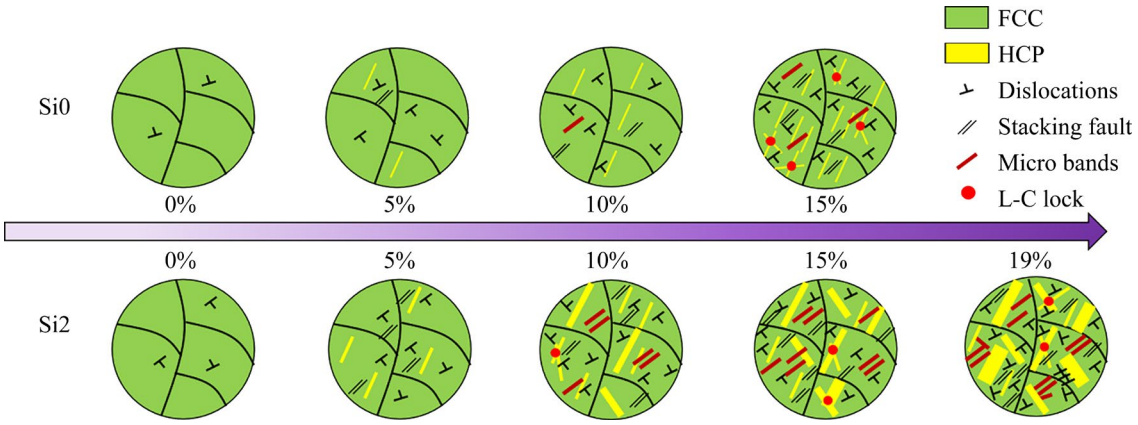

Fig. 9 Schematic sketches illustrating deformation mechanism transitions and features of deformed microstructures in Si0 and Si2 HEAs at 77 K

force) [6]. The earlier FCC−HCP MT indicated that Si2 HEAs can generate HCP in a larger strain range, resulting in superior mechanical properties. Second, the decrease in the SFE increased the transformation rate of the FCC−HCP MT, which further promoted the FCC−HCP MT. In fact, there is a critical strain range for the dislocation-dominated deformation mechanism. The strain hardening rates of the two alloys are almost the same in the first 5% strain range. As the strain increased to 10%, EBSD and TEM results showed that the MT rate of Si2 HEAs is significantly accelerated, and the strain hardening rate also increased. That is, when the critical strain range is exceeded, MT accelerates and significantly increases the strain-hardening rate, which is similar to that of traditional TRIP steel [51]. Our results also clearly show that the dislocations of Si0 HEAs and a small amount of MT can only provide limited work hardening, and rapid MT and high-density HCP guarantee continuous work hardening of Si2 HEAs.

The TEM results showed that there were more MBs in the Si2 HEAs, which were mainly attributed to the planar slip of the dislocations. The lower SFE in the Si2 HEAs led to wide extended dislocations, which were not conducive to the cross-slip of dislocations. Similar studies have shown that the addition of interstitial carbon to HEAs reduces the SFE and increases the lattice friction stress, both of which can inhibit the cross-slip of dislocations, resulting in a plane slip. MBs are usually plate-like structures with a high dislocation density arranged along the {111} plane in FCC metals. The MBs formation process in this study is similar to the microstrip formation mechanism in the tensile process of high-Mn light steel, as studied by WELSH et al [52]. A low SFE results in the activation of plane slip at an early stage of deformation. The post-activated dislocation propagated in the sliding plane, resulting in the formation of an initial plane slip band that passed through the grain and eventually reached the grain boundary. The gradual accumulation of dislocations provides back stress, resulting in the emission of more dislocations in the slip band. Therefore, a fully developed slip band called an MB is formed. The MBs formed in the grains become obstacles in the subsequent dislocation slip path, thereby enhancing the strain-hardening capacity. The development of the MBs structure was similar to that of in situ grain refinement, in which each MBs acted as a low-angle grain boundary and reduced the dislocation-free path [53]. Therefore, compared with Si0 HEAs, the increase in microstrip events in Si2 HEAs led to an increase in the work-hardening ability under continuous strain. This is called MB-induced plasticity and is considered to have effects similar to those of TWIP and TRIP.

In addition, a fixed L-C lock was generated via the intersection of HCP phases in the deformed microstructures of the two alloys. Since the density of the L-C lock is relatively lower than that of ε-HCP and MBs, the L-C lock can partially promote the extreme strain hardening of HEA. Previous studies [54] have shown that L-C locks not only hinder the movement of dislocations but also act as Frank–Read sources for dislocation propagation, resulting in stable progressive strain hardening. The role of the L-C lock in strain hardening is mainly due to its ability to accumulate dislocations. The L-C lock strongly hinders dislocation slip, which is an effective barrier to the accumulation of dislocations and can produce effective strain hardening.

5 Conclusions

(1) Metastable HEAs were successfully prepared by SLM. Both the Si-free and Si-added HEAs had single-phase FCC structures. The addition of Si reduced the grain size.

(2) The HEAs prepared by SLM exhibited not only non-brittleness at 77 K but also excellent strength and ductility. Compared with Si0 HEAs, the tensile strength and ductility of Si2 HEAs are improved by 53.1% and 58%, respectively. This is mainly attributed to the large lattice distortion and low SFE caused by the Si addition, and these characteristics are more remarkable at 77 K.

(3) Transformation-induced plasticity (TRIP) was the main deformation mode, in addition to dislocation slip. The martensitic transformation rate was high throughout the deformation process, and the cryogenic temperature and low SFE caused the martensitic transformation rate of the Si2 HEAs to be significantly faster than that of the Si0-HEAs.

(4) The high strain hardening of Si2 HEAs is caused by the continued enhancement of TRIP effect and the interaction of ε-HCP, microbands,

and L-C locks with dislocations, and maintains dynamic strain distribution during deformation. This ultra-high strain hardening significantly enhanced the strength and ductility.

CRediT authorship contribution statement

Zhan-jiang LI: Conceptualization, Methodology, Writing − Original draft; **Yi-xi HOU:** Conceptualization, Methodology; **Li CHEN** and **Qing-xin CHEN:** Investigation, Resources; **Jun-feng CHEN:** Data curation, Writing − Review & editing; **Fa CHANG:** Data curation, Formal analysis; **Pin-qiang DAI** and **Qun-hua TANG:** Resources, Project administration.

Declaration of competing interest

The authors declare that they have no known competing financial interests or personal relationships that could have appeared to influence the work reported in this paper.

Acknowledgments

This work was supported by Program for Innovative Research Team in Science and Technology in Fujian Province University, China, and the Natural Science Foundation of Fujian Province, China (Nos. 2023J011013, 2020J01898).

Data Availability

The raw/processed data required to reproduce these findings cannot be shared at this time due to technical or time limitations.

References

[1] MOGHADDAM A O, SHABUROVA N A, SAMODUROVA M N, ABDOLLAHZADEH A, TROFIMOV E A. Additive manufacturing of high entropy alloys: A practical review [J]. Journal of Materials Science & Technology, 2021, 77: 131−162.

[2] ZHANG Z J, MAO M M, WANG J W, GLUDOVATZ B, ZHANG Z, MAO S X, GEORGE E P, YU Q, RITCHIE R O. Nanoscale origins of the damage tolerance of the high-entropy alloy CrMnFeCoNi [J]. Nature Communications, 2015, 6: 10143.

[3] GAO Xu-zhou, LU Yi-ping, ZHANG Bo, LIANG Ning-ning, WU Guan-zhong, SHA Gang, LIU Ji-zi, ZHAO Yong-hao. Microstructural origins of high strength and high ductility in an $AlCoCrFeNi_{2.1}$ eutectic high-entropy alloy [J]. Acta Materialia, 2017, 141: 59−66.

[4] ZHANG T W, MA S G, ZHAO D, WU Y C, ZHANG Y, WANG Z H, QIAO J W. Simultaneous enhancement of strength and ductility in a NiCoCrFe high-entropy alloy upon dynamic tension: Micromechanism and constitutive modeling [J]. International Journal of Plasticity, 2020, 124: 226−246.

[5] LIN Dan-yang, XU Lian-yong, JING Hong-yang, HAN Yong-dian, ZHAO Lei, MINAMI F. Effects of annealing on the structure and mechanical properties of FeCoCrNi high-entropy alloy fabricated via selective laser melting [J]. Additive Manufacturing, 2020, 32: 101058.

[6] LAPLANCHE G, KOSTKA A, REINHART C, HUNFELD J, EGGELER G, GEORGE E P. Reasons for the superior mechanical properties of medium-entropy CrCoNi compared to high-entropy CrMnFeCoNi [J]. Acta Materialia, 2017, 128: 292−303.

[7] AN Zi-bing, MAO Sheng-cheng, LIU Yi-nong, YANG Lu-yan, VAYYALA A, WEI Xiao, LIU Cheng, SHI Cai-juan, JIN Hui-xin, LIU Cui-xiu, ZHANG Jian-xin, ZHANG Ze, HAN Xiao-dong. Inherent and multiple strain hardening imparting synergistic ultrahigh strength and ductility in a low stacking faulted heterogeneous high-entropy alloy [J]. Acta Materialia, 2023, 243: 118516.

[8] LOPES J G, AGRAWAL P, SHEN Jia-jia, SCHELL N, MISHRA R S, OLIVEIRA J P. Evolution of microstructure and mechanical properties in gas tungsten arc welded dual-phase $Fe_{50}Mn_{30}Co_{10}Cr_{10}$ high entropy alloy [J]. Materials Science and Engineering: A, 2023, 878: 145233.

[9] SHEN Jia-jia, AGRAWAL P, RODRIGUES T A, LOPES J G, SCHELL N, HE Jing-jing, ZENG Zhi, MISHRA R S, OLIVEIRA J P. Microstructure evolution and mechanical properties in a gas tungsten arc welded $Fe_{42}Mn_{28}Co_{10}Cr_{15}Si_5$ metastable high entropy alloy [J]. Materials Science and Engineering: A, 2023, 867: 144722.

[10] ZHAO Jia-qi, TIAN Hua, WANG Zhong, WANG Xue-jiao, QIAO Jun-wei. FCC-to-HCP phase transformation in $CoCrNi_x$ medium-entropy alloys [J]. Acta Metallurgica Sinica (English Letters), 2020, 33(8): 1151−1158.

[11] LI Zhi-ming, PRADEEP K G, DENG Yun, RAABE D, TASAN C C. Metastable high-entropy dual-phase alloys overcome the strength-ductility trade-off [J]. Nature, 2016, 534(7606): 227−230.

[12] PARK J M, ASGHARI-RAD P, ZARGARAN A, BAE J W, MOON J G, KWON H, CHOE J G, YANG S S, YU J H, KIM H S. Nano-scale heterogeneity- driven metastability engineering in ferrous medium-entropy alloy induced by additive manufacturing [J]. Acta Materialia, 2021, 221: 117426.

[13] BAJAJ P, HARIHARAN A, KINI A, KÜRNSTEINER P, RAABE D, JÄGLE E A. Steels in additive manufacturing: A review of their microstructure and properties [J]. Materials Science and Engineering: A, 2020, 772: 138633.

[14] GLUDOVATZ B, HOHENWARTER A, CATOOR D, CHANG E H, GEORGE E P, RITCHIE R O. A fracture-resistant high-entropy alloy for cryogenic applications [J]. Science, 2014, 345(6201): 1153−1158.

[15] HUANG Shuo, LI Wei, LU Song, TIAN Fu-yang, SHEN Jiang, HOLMSTRÖM E, VITOS L. Temperature dependent stacking fault energy of FeCrCoNiMn high entropy alloy [J]. Scripta Materialia, 2015, 108: 44−47.

[16] WANG Ming, SONG Bo, WEI Qing-song, ZHANG Yuan-jie, SHI Yu-sheng. Effects of annealing on the microstructure and mechanical properties of selective laser melted AlSi7Mg alloy [J]. Materials Science and Engineering: A, 2019, 739:

463−472.

[17] HOU Yi-xi, LIU Tao, HE Dong-dong, LI Zhan-jiang, CHEN Li, SU Hong-hong, FU Pei-xin, DAI Pin-qiang, HUANG Wei-dong. Sustaining strength-ductility synergy of SLM $Fe_{50}Mn_{30}Co_{10}Cr_{10}$ metastable high-entropy alloy by Si addition [J]. Intermetallics, 2022, 145: 107565.

[18] CHANG H, ZHANG T W, MA S G, ZHAO D, XIONG R L, WANG T, LI Z Q, WANG Z H. Novel Si-added CrCoNi medium entropy alloys achieving the breakthrough of strength-ductility trade-off [J]. Materials & Design, 2021, 197: 109202.

[19] WEI Dai-xiu, GONG Wu, TSURU T, LOBZENKO I, LI Xiao-qing, HARJO S, KAWASAKI T, DO H S, BAE J W, WAGNER C, LAPLANCHE G, KOIZUMI Y, ADACHI H, AOYAGI K, CHIBA A, LEE B J, KIM H S, KATO H. Si-addition contributes to overcoming the strength-ductility trade-off in high-entropy alloys [J]. International Journal of Plasticity, 2022, 159: 103443.

[20] LIN Dan-yang, XI Xin, LI Xiao-jie, HU Ji-xu, XU Lian-yong, HAN Yong-dian, ZHANG Yan-kun, ZHAN Lei. High-temperature mechanical properties of FeCoCrNi high-entropy alloys fabricated via selective laser melting [J]. Materials Science and Engineering: A, 2022, 832: 142354.

[21] DUAN Heng, LIU Bin, FU Ao, HE Jun-yang, YANG Tao, LIU C T, LIU Yong. Segregation enabled outstanding combination of mechanical and corrosion properties in a FeCrNi medium entropy alloy manufactured by selective laser melting [J]. Journal of Materials Science & Technology, 2022, 99: 207−214.

[22] LIN W C, CHANG Y J, HSU T H, GORSSE S, SUN F, FURUHARA T, YEH A C. Microstructure and tensile property of a precipitation strengthened high entropy alloy processed by selective laser melting and post heat treatment [J]. Additive Manufacturing, 2020, 36: 101601.

[23] KALSAR R, KHANDAL P, SUWAS S. Effects of stacking fault energy on deformation mechanisms in Al-added medium Mn TWIP steel [J]. Metallurgical and Materials Transactions A, 2019, 50(8): 3683−3696.

[24] LIU Jun-peng, GUO Xiao-xiang, LIN Qing-yun, HE Zhan-bing, AN Xiang-hai, LI Lai-feng, LIAW P K, LIAO Xiao-zhou, YU Li-ping, LIN Jun-pin, XIE Lu, REN Jing-li, ZHANG Yong. Excellent ductility and serration feature of metastable CoCrFeNi high-entropy alloy at extremely low temperatures [J]. Science China Materials, 2019, 62(6): 853−863.

[25] CHEN Si-jing, OH H S, GLUDOVATZ B, KIM S J, PARK E S, ZHANG Ze, RITCHIE R. O, YU Qian. Real-time observations of TRIP-induced ultrahigh strain hardening in a dual-phase CrMnFeCoNi high-entropy alloy [J]. Nature Communications, 2020, 11(1): 826.

[26] BEAUSIR B, FUNDENBERGER J J. Analysis tools for electron and X-ray diffraction, ATEX-software [Z]. www.atex-software.eu, Universit´e de Lorraine - Metz.

[27] ZHU Yun-tian, AMEYAMA K, ANDERSON P M, BEYERLEIN I J, GAO Hua-jian, KIM H S, LAVERNIA E, MATHAUDHU S, MUGHRABI H, RITCHIE R O, TSUJI N, ZHANG Xiang-yi, WU Xiao-lei. Heterostructured materials: superior properties from hetero-zone interaction [J]. Materials Research Letters, 2021, 9(1): 1−31.

[28] BAE J W, JUNG J, KIM J G, PARK J M, HARJO S, KAWASAKI T, WOO W, KIM H S. On the phase transformation and dynamic stress–strain partitioning of ferrous medium-entropy alloy using experimentation and finite element method [J]. Materialia, 2020, 9: 100619.

[29] ZHANG D D, ZHANG J Y, KUANG J, LIU G, SUN J. Superior strength-ductility synergy and strain hardenability of Al/Ta Co-doped NiCoCr twinned medium entropy alloy for cryogenic applications [J]. Acta Materialia, 2021, 220: 117288.

[30] TANG Lei, YAN Kun, CAI Biao, WANG Yi-qiang, LIU Bin, KABRA S, ATTALLAH M M, LIU Yong. Deformation mechanisms of $FeCoCrNiMo_{0.2}$ high entropy alloy at 77 and 15 K [J]. Scripta Materialia, 2020, 178: 166−170.

[31] PICAK S, LIU J, HAYRETTIN C, NASIM W, CANADINC D, XIE K, CHUMLYAKOV Y I, KIREEVA I V, KARAMAN I. Anomalous work hardening behavior of $Fe_{40}Mn_{40}Cr_{10}Co_{10}$ high entropy alloy single crystals deformed by twinning and slip [J]. Acta Materialia, 2019, 181: 555−569.

[32] PAN Zhi-min, LUO Hong, CHENG Hong-xu, ZHAO Qian-cheng, WANG Xue-fei, FU Yu, MA Yi-cong, LI Xiao-gang. A nano-sized precipitate strengthened medium entropy alloy with superior strength-ductility synergy and exceptional corrosion resistance [J]. Materials Today Physics, 2023, 33: 101062.

[33] SHIH M, MIAO Jia-shi, MILLS M, GHAZISAEIDI M, Stacking fault energy in concentrated alloys [J]. Nature Communications, 2021, 12(1): 3590.

[34] ZHANG Y H, ZHUANG Y, HU A, KAI J J, LIU C T. The origin of negative stacking fault energies and nano-twin formation in face-centered cubic high entropy alloys [J]. Scripta Materialia, 2017, 130: 96−99.

[35] LI Su-ning, WITHERS P J, KABRA S, YAN Kun. The behaviour and deformation mechanisms for 316L stainless steel deformed at cryogenic temperatures [J]. Materials Science and Engineering: A, 2023, 880: 145279.

[36] THORNTON P R, MITCHELL T E, HIRSCH P B. The dependence of cross-slip on stacking-fault energy in face-centred cubic metals and alloys [J]. Philosophical Magazine, 1962, 7(80): 1349−1369.

[37] JO M, KOO Y M, LEE B J, JOHANSSON B, VITOS L, KWON S K. Theory for plasticity of face-centered cubic metals [J]. Proceedings of the National Academy of Sciences of the United States of America, 2014, 111(18): 6560−6565.

[38] YANG Zhi-biao, LU Song, TIAN Yan-zhong, GU Zi-jian, SUN Jian, VITOS L. Theoretical and experimental study of phase transformation and twinning behavior in metastable high-entropy alloys [J]. Journal of Materials Science & Technology, 2022, 99: 161−168.

[39] YANG Zhi-biao, LU Song, TIAN Yan-zhong, GU Zi-jian, MAO Hua-hai, SUN Jian, VITOS L. Assessing the magnetic order dependent γ-surface of Cr−Co−Ni alloys [J]. Journal of Materials Science & Technology, 2021, 80: 66−74.

[40] LU Song, SUN Xun, TIAN Yan-zhong, AN Xiang-hai, LI Wei, CHEN Yu-jie, ZHANG Hua-lei, VITOS L. Theory of transformation-mediated twinning [J]. PNAS Nexus, 2023, 2(1): pgac282.

[41] BAE J W, SEOL J B, MOON J, SOHN S S, JANG Min-ji, UM H Y, LEE B J, KIM H S. Exceptional phase-

transformation strengthening of ferrous medium-entropy alloys at cryogenic temperatures [J]. Acta Materialia, 2018, 161: 388−399.
[42] PARK J M, CHOE J H, PARK H K, SON S, JUNG J, KIM T S, YU J H, KIM J G, KIM H S. Synergetic strengthening of additively manufactured (CoCrFeMnNi)-99C_1 high-entropy alloy by heterogeneous anisotropic microstructure [J]. Additive Manufacturing, 2020, 35: 101333.
[43] WU Z, BEI H, PHARR G M, GEORGE E P. Temperature dependence of the mechanical properties of equiatomic solid solution alloys with face-centered cubic crystal structures [J]. Acta Materialia, 2014, 81: 428−441.
[44] SU Jing, RAABE D, LI Zhi-ming. Hierarchical microstructure design to tune the mechanical behavior of an interstitial TRIP-TWIP high-entropy alloy [J]. Acta Materialia, 2019, 163: 40−54.
[45] HE J Y, WANG H, HUANG H L, XU X D, CHEN M W, WU Y, LIU X J, NIEH T G, AN K, LU Z P. A precipitation-hardened high-entropy alloy with outstanding tensile properties [J]. Acta Materialia, 2016, 102: 187−196.
[46] GUO Lin, OU Xiao-qin, NI Song, LIU Yong, SONG Min. Effects of carbon on the microstructures and mechanical properties of FeCoCrNiMn high entropy alloys [J]. Materials Science and Engineering: A, 2019, 746: 356−362.
[47] ZHAO Y H, LIAO X Z, JIN Z, VALIEV R Z, ZHU Y T. Microstructures and mechanical properties of ultrafine grained 7075 Al alloy processed by ECAP and their evolutions during annealing [J]. Acta Materialia, 2004, 52(15): 4589−4599.
[48] WANG Xiao-di, ZHANG Zhe, WANG Zheng-bin, REN Xue-chong. Excellent tensile property and its mechanism in Al0.3CoCrFeNi high-entropy alloy via thermo-mechanical treatment [J]. Journal of Alloys and Compounds, 2022, 897: 163218.
[49] SHI Rong-jian, MA Yuan, WANG Zi-dong, GAO Lei, YANG Xu-Sheng, QIAO Li-jie, PANG Xiao-lu. Atomic-scale investigation of deep hydrogen trapping in NbC/α-Fe semi-coherent interfaces [J]. Acta Materialia, 2020, 200: 686−698.
[50] WEI Cheng-bin, LU Yi-ping, DU Xing-hao, LI Ting-ju, WANG Tong-min, LIAW P K. Remarkable strength of a non-equiatomic Co29Cr29Fe29Ni12.5W0.5 high-entropy alloy at cryogenic temperatures [J]. Materials Science and Engineering: A, 2021, 818: 141446.
[51] SUN Sheng-hui, CAI Ming-hui, DING Hua, HUANG Hong-shou, PAN Hai-jun. Deformation mechanisms of a novel Mn-based 1 GPa TRIP/TWIP assisted lightweight steel with 63% ductility [J]. Materials Science and Engineering: A, 2021, 802: 140658.
[52] WELSCH E, PONGE D, HAFEZ HAGHIGHAT S M, SANDLÖBES S, CHOI P, HERBIG M, ZAEFFERER S, RAABE D. Strain hardening by dynamic slip band refinement in a high-Mn lightweight steel [J]. Acta Materialia, 2016, 116: 188−199.
[53] LI Na, CHEN Wen-tian, HE Jun-yang, GU Ji, WANG Zhang-wei, LI Yue, SONG Min. Dynamic deformation behavior and microstructure evolution of CoCrNiMo_x medium entropy alloys [J]. Materials Science and Engineering: A, 2021, 827: 142048.
[54] FAN Lei, YANG Tao, ZHAO Yi-lu, LUAN Jun-hua, ZHOU Gang, WANG Hao, JIAO Zeng-bao, LIU Chain-tsuan. Ultrahigh strength and ductility in newly developed materials with coherent nanolamellar architectures [J]. Nature Communications, 2020, 11(1): 6240.

通过强化 TRIP 效应实现低温下 Si 添加亚稳态高熵合金的优异强度–延展性协同

李战江[1,2,3]，侯毅熙[4]，陈 丽[1,2]，陈庆鑫[2,3]，陈俊锋[1]，常 发[2,3]，戴品强[1,2,3]，唐群华[5]

1. 福州大学 材料科学与工程学院，福州 350116；
2. 福建理工大学 材料科学与工程学院，福州 350118；
3. 福建省先进材料加工与应用重点实验室，福州 350108；
4. 北京工业大学 材料与制造学院 先进材料微观结构与性能北京市重点实验室，北京 100124；
5. 莆田学院 机电工程学院，莆田 351100

摘 要：研究通过选择性激光熔融法制备的$(Fe_{50}Mn_{30}Co_{10}Cr_{10})_{100-x}Si_x$ (x=0 (Si0), 2 (Si2))亚稳高熵合金(HEA)的低温拉伸行为。结果表明，Si 的加入会导致晶格畸变和层错能的降低，尤其是在 77 K 时，这极大地促进了 Si2 HEA 的相变诱导塑性效应(TRIP)。Si2-HEAs 的屈服强度、抗拉强度和延展性分别为 505.2 MPa、1364.1 MPa 和 19%，比 Si0 合金分别高 43%、53%和 58%。TRIP 是位错滑移之外的主要变形模式，在强化过程中起着关键作用。强化和持续的 TRIP 保持了变形过程中的动态应变分布。这种超高应变硬化大大提高了合金的强度和延展性。

关键词：$Fe_{50}Mn_{30}Co_{10}Cr_{10}$ 高熵合金；选区激光熔化；低温；Si 添加；相变诱导塑性(TRIP)效应

(Edited by Xiang-qun LI)